Graph Neural Network-Based Multi-Objective Optimization for Renewable Energy Spatial Layout Design

Jing Xu
Zhengzhou University of Light Industry, Zhengzhou City, Henan Province, 450000, China
E-mail: gtea0086@126.com

Keywords: graph neural network, renewable energy, multi-objective dynamic optimization, spatial element identification and optimal layout, ecological conflict control

Received: July 3, 2025

With the rapid development of Renewable Energy (RE), traditional layout methods struggle to integrate multi-source geographic data and avoid ecological conflicts. To address these issues, this paper proposes an intelligent solution combining a Graph Neural Network (GNN) and a multi-objective dynamic optimization framework to enhance planning accuracy and layout efficiency. Based on 1 km×1 km grid data of wind farms in northwest China (15,600 nodes/156×100 km²) and photovoltaic parks in eastern China (12,800 nodes/128×100 km²), a geographic spatial graph is constructed, allowing GNNs to identify spatial elements precisely. The framework integrates Genetic Algorithms (GA) with a Double Deep Q-Network (DDQN) to optimize RE layouts, balancing power generation efficiency, ecological impact, and construction costs through multi-objective dynamic optimization. Case studies of wind farms in northwest China and photovoltaic parks in eastern China are used to validate robustness and adaptability under complex terrains. Results show the proposed method achieves a spatial recognition accuracy of 0.93, 14.8% higher than traditional Convolutional Neural Networks (CNNs), ecological conflicts reduced by 29.6%, and cost savings reached 17.2%. This identification-optimization closed-loop framework effectively processes non-Euclidean spatial data and performs multi-objective collaborative optimization.

Povzetek: Kako znanstveno podpreti načrtovanje vetrnih in sončnih polj z večciljno, dinamično optimizacijo ob različnih terenih in omejitvah? Okvir GNN+GA-DDQN za prostorsko postavitev OVE iz neevklidskih podatkov izboljša prepoznavo elementov, zmanjša ekološke konflikte in stroške.

1 Introduction

As an essential support for achieving the “dual carbon” goals, the deployment of RE is accelerating around the world [1], [2], [3], [4]. Wind and solar energy have become the focus of development due to their cleanliness and broad distribution base, but in the actual layout process, they often face multiple constraints such as firm heterogeneity of geographical resources, complex distribution of ecologically sensitive areas, and variable construction costs [5], [6], [7]. Traditional methods have difficulty handling non-Euclidean spatial relationships, especially in the intelligent identification of spatial distribution and layout optimization. They cannot dynamically respond to changes in environmental design elements, causing the site selection and layout results to deviate from the optimal solution. A new intelligent method is urgently needed to accurately perceive multi-source factors at the spatial level and perform collaborative optimization to support the scientific site selection and environmentally friendly layout of green energy projects [8], [9].

This paper focuses on the site selection and equipment layout optimization of wind farms and PV power stations. Such problems require weighing multi-dimensional constraints such as resource endowment, land use, grid access, and ecological protection in complex geographical spaces, which directly affect the economic efficiency and sustainability of the project throughout its life cycle. The core challenge of current RE environmental design is accurately identifying spatial elements and multi-objective coordinated optimization through technical means. How to effectively identify the complex boundaries between resource-rich and ecologically sensitive areas and construct an identification model that can express spatial topological relationships has become a key technical problem that affects layout accuracy. To address this problem, Rane et al. and Gerbo et al. [10], [11] adopted a multi-criteria suitability analysis method based on Geographic Information System (GIS) to comprehensively evaluate the feasibility of building a PV power station. However, there were problems such as strong subjectivity in weight setting and failure to consider dynamic environmental changes fully. Günen, Ajanaku and Strager [12], [13] combined GIS with multi-criteria decision-making methods to evaluate the optimal location of RE sources. However, the model was sensitive to weight distribution and did not fully consider geographical constraints. Wang Z [14] proposed an adaptive convolutional residual network model, which combined project risk classification and electricity price regression prediction, combined novel preprocessing technology and feature optimization, and achieved strong adaptability and reliability in renewable energy electricity price prediction, providing an independent high-performance solution for energy market planning. Most of these methods focus on power generation prediction or static evaluation and lack the discussion of the "identification-optimization" closed-loop mechanism in spatial layout optimization problems. Existing research on spatial suitability evaluation is divided into two categories: a static evaluation model based on GIS and fuzzy decision-making methods, and a modeling method that relies on machine learning models. For example, Effat and El-Zeiny, and Genç et al. [15], [16] used remote sensing data, geospatial models, or GIS to delineate and map potential solar and wind energy areas, thereby constructing suitable sites. Although these studies have promoted the development of the field, they still have significant limitations in multi-source data fusion and eco-efficiency coordinated optimization. In particular, they cannot model non-Euclidean adjacency relationships between spatial elements, making it difficult to deal with the problem of expressing coupled characteristics across terrains and resource types in wind power and PV site selection [17]. Existing studies have mostly used GIS spatial analysis [18], [19], [20], random forest classification [21], [22], or CNN algorithms for suitability evaluation [23], but they have significant limitations. Zheng et al. [24] used an integer GA with an adaptive strategy to optimize the layout of wind farms, but there were problems of slow convergence or local optimality. Li et al. [25] proposed a method that combined federated learning with least squares generative adversarial networks to generate high-quality RE scenarios. Wang et al. and Zuo et al. [26], [27] divided wind farm areas based on fuzzy clustering, but the classification results were sensitive to the initial parameters. Eroğlu [28] used a method that combined GIS with fuzzy hierarchical analysis to generate a suitability map and identify optimal and restricted areas, thereby improving the accuracy of site selection. Deveci et al. [29] used the Full Coordination (FUCOM) weighting method based on q-Rung Orthopair Fuzzy Sets (q-ROFSs) and the Combined Compromise Solution (CoCoSo) decision model to optimize the candidate sites for four floating offshore wind farms in Norway. The model was verified to be stable through a sensitivity analysis. Fu et al. [30] attempted to use machine learning to predict resource distribution, but the generalization ability of the model was limited by the regional representativeness of the training data; Tinsley et al., Wang and Li, and Sahoo and Sethi [31], [32], [33], proposed that the development of RE cannot be at the expense of the ecological environment, resulting in a significant reduction in the available areas. Song et al. [34] proposed a wind power prediction method that combined Graph Convolutional Networks (GCNs) and multi-resolution CNNs to integrate spatial and temporal features to improve prediction accuracy. Although the above methods have improved the evaluation capabilities in different dimensions, their static structure and single objective make them difficult to adapt to the needs of highly dynamic and strongly coupled complex geographical systems, and they lack a modeling mechanism for the trade-off between power generation efficiency, ecological interference, and cost constraints.

This paper innovatively proposes a collaborative framework based on GNN and multi-objective dynamic optimization. Through Gaussian weighted adjacency matrix and multi-head attention mechanism, a dynamic spatial graph structure is constructed to break through the limitations of traditional GIS static weight allocation and CNN boundary effect; a GA-reinforcement learning hybrid optimizer is designed, and Pareto frontier search is used to realize real-time interaction between ecological sensitivity weight and resource potential mapping, which increases the reduction of environmental conflicts from 12.0% of CNN to 29.6%. In comparison, the layout efficiency is improved by 21.4%. Compared with classic multi-objective evolutionary algorithms such as Non-dominated Sorting Genetic Algorithm II (NSGA-II), this method optimizes the convergence speed in cross-regional migration scenarios. It maintains a high diversity of solution sets, demonstrating global optimization capabilities in complex environments. Experiments show that the framework has improved accuracy in the cross-regional migration of wind farms in the northwest plains and PV parks in the eastern river network, and its convergence speed is faster than NSGA-II. It provides a technical path that considers both efficiency and ecological protection for the layout of RE in complex geographical scenarios. It also solves the core bottlenecks of existing models in non-Euclidean data modeling and multi-objective collaboration. The relevant comparison is shown in Table 1.

This paper raises the core research question: Can the GNN and GA-DDQN collaborative framework significantly improve the accuracy, efficiency and ecological compatibility of renewable energy layout under multiple ecological constraints? Specific hypotheses include: Gaussian weighted adjacency matrix and multi-head attention mechanism can improve the accuracy of spatial element recognition; GA-DRL hybrid optimizer can accelerate convergence and reduce ecological conflicts; dynamic weight mechanism can balance power generation efficiency and ecological cost.

Table 1: Comparison of optimization methods for spatial layout of renewable energy sources

Method Category	Core Task	Main Limitation	Solution Proposed in This Paper	Dataset
GIS Multi-Criteria Decision	Static suitability analysis	Subjective weighting; ignores dynamic changes	Dynamic graph structure +adaptive weights	Regional scale
Random Forest/CNN	Resource distribution prediction	Lacks spatial topology modeling	GNN with multi-head attention mechanism	Landsat remote sensing imagery
Integer Genetic Algorithm	Layout optimization	Slow convergence; prone to local optima	GA-DRL hybrid optimizer	Simulated wind farm
Fuzzy Clustering Partition	Wind farm zoning	Sensitive to initial parameters	Dynamic weight adjustment mechanism	Offshore wind farm
Method in this paper	Identification–optimization collaboration	Overcomes existing limitations	GNN + GA-DRL dynamic framework	Measured data from Northwest/Eastern China

2 Algorithm design

2.1 Construction of geospatial graph structure

To realize the spatial distribution modeling of RE environmental design elements, the study area is divided into regular grid units of 1 km × 1 km, and each unit is used as an independent node in the graph structure. The grid division adopts an equal-area azimuthal projection to eliminate the deformation effect of high-latitude areas. The node attribute dimensions include terrain slope, wind speed, light intensity, land use type, ecological sensitivity index, and traffic accessibility, a total of 6 core indicators. All attributes are normalized by Z-score to eliminate dimensional differences and input as node feature vectors.

The adjacency relationship between nodes is constructed through the spatial adjacency matrix. A hybrid strategy is used to determine the connection rules: for plain and hilly areas, an 8-neighborhood connection is established based on the Euclidean distance threshold of 2 km; for mountainous and river-dense areas, the K-nearest neighbor algorithm is used to dynamically adjust the number of neighbors to avoid false associations caused by terrain barriers. The neighbor weights are calculated using the Gaussian kernel function:

$$w_{ij} = \exp\left(-\frac{d_{ij}^2}{2\sigma^2}\right) \quad (1)$$

In Formula (1), d_{ij}^2 is the geographical distance between nodes i and j (km), and σ is set to 1.5 times the average grid spacing of the region. This design strengthens the local spatial autocorrelation while weakening the noise interference of distant nodes.

To improve the expression ability of ecological spatial structure, a composite edge weight design based on the connectivity of environmental corridors is introduced: based on the original Gaussian weighting, the ecological connectivity correction coefficient λ_{ij} is introduced, and the composite edge weight is defined as:

$$w_{ij}^* = \lambda_{ij} \cdot w_{ij} \quad (2)$$

In Formula (2), λ_{ij} assigns a correction weight between 0.8 and 1.2 according to whether there is an ecological corridor between nodes, which enhances the modeling effect of boundary connectivity in ecologically sensitive areas.

The graph structure verification uses a joint evaluation of cross-entropy loss and Moran's index: a 10-fold cross-validation is performed on wind speed and light attributes.

2.2 Multimodal feature coding and spatial element identification

2.2.1 Environmental element recognition

Based on the constructed geospatial graph structure, the Graph Attention Network (GAT) is used to realize the feature encoding of multi-source heterogeneous attributes and the propagation of neighborhood information. The model adopts a three-level stacked architecture, including an input, intermediate propagation, and output layers. The propagation layer is configured as a two-layer GAT module, and each layer contains 8 parallel attention heads to enhance the robustness of feature extraction. Feature encoding maps the original node attributes to a high-dimensional space through an embedding matrix:

$$h_i^{(0)} = W_{emb} \cdot x_i \tag{3}$$

In Formula (3), $x_i \in \mathbb{R}^{10}$ is the standardized attribute vector of node i ; $W_{emb} \in \mathbb{R}^{64\times10}$ is the learnable embedding matrix; $h_i^{(0)} \in \mathbb{R}^{64}$ is the initial feature representation. Neighborhood information propagation is achieved through a multi-head attention mechanism. The calculation process of the L-layer GAT is as follows:

The attention weight is calculated as follows:

$$e_{ij}^{(l)} = \text{LeakyReLU}(a^{(l)T} \cdot [W^{(l)}h_i^{(l-1)}||W^{(l)}h_j^{(l-1)}]) \tag{4}$$

$$\alpha_{ij}^{(l)} = \frac{\exp(e_{ij}^{(l)})}{\sum_{k\in\mathcal{N}(i)} \exp(e_{ik}^{(l)})} \tag{5}$$

Here, $W^{(l)} \in \mathbb{R}^{64\times64}$ is the linear transformation matrix; $a^{(l)} \in \mathbb{R}^{128}$ is the attention parameter vector; $||$ represents the vector concatenation operation; $\mathcal{N}(i)$ is the neighbor set of node i.

This step dynamically allocates the contribution weights of neighboring nodes through learnable parameters, breaking through traditional GCN's fixed average aggregation mode.

The feature updates are as follows:

$$h_i^{(l)} = \sigma(\frac{1}{K}\sum_{k=1}^{K}\sum_{j\in\mathcal{N}(i)} \alpha_{ij}^{(l,k)}W^{(l,k)}h_j^{(l-1)}) \tag{6}$$

In Formula (6), K is the number of attention heads; σ is the ELU activation function; $W^{(l,k)} \in \mathbb{R}^{64\times64}$ is the parameter matrix of the k-th head. This module identifies environmental constraints, such as ecologically sensitive areas, terrain barrier areas, and high ecological cost areas. The final output, a 64-dimensional node vector, is mapped into a 32-dimensional heat map vector $Z_i \in \mathbb{R}^{32}$ through a fully connected layer, which is used for visual identification of spatial element distribution and subsequent optimization analysis. The identification results are presented as an ecological constraint intensity heat map, as shown in Fig. 1.

The feature fusion strategy uses standard residual connections and layer normalization to improve training stability:

$$h_i^{(l)} = \text{LayerNorm}\left(h_i^{(l-1)} + \text{Dropout}\left(\sigma\left(\sum_{j\in\mathcal{N}(i)} \alpha_{ij}^{(l)}W^{(l)}h_j^{(l-1)}\right)\right)\right) \tag{7}$$

This mechanism efficiently characterizes heterogeneous ecological areas through the attention mechanism, significantly improving the accuracy of environmental boundary identification under complex terrain.

Residual connections alleviate the gradient vanishing problem; Dropout suppresses overfitting; layer normalization ensures feature distribution consistency. The final output layer maps the 64-dimensional features to the target space through a fully connected layer:

$$z_i = W_{out} \cdot h_i^{(2)} \tag{8}$$

In Formula (8), $z_i \in \mathbb{R}^{32}$ is the high-dimensional spatial feature vector of node i, which serves as the input of the multi-objective optimization module.

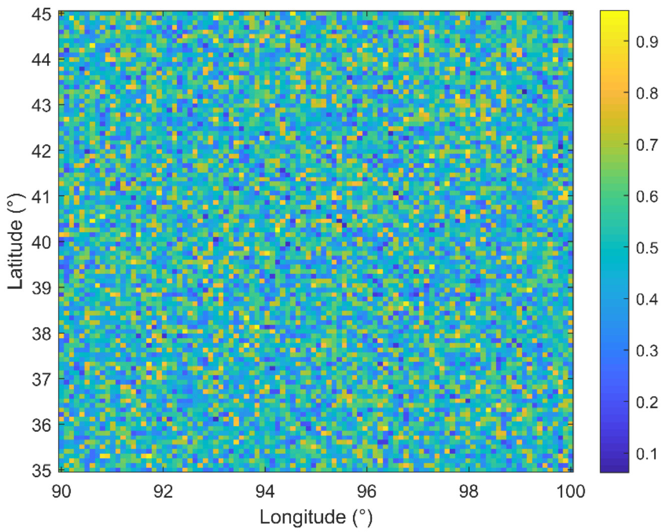

Figure 1: Ecological environment constraints heat map

The geospatial map structure shown in Fig. 1 demonstrates the spatial distribution characteristics of RE environmental design elements in the study area. Its environmental design elements include six indicators, such as slope, soil bearing capacity, and ecological sensitivity). The heat map uses Projected coordinate system (unit: kilometers) as coordinate axes to map the comprehensive environmental constraint intensity of each 1 km×1 km grid unit. It is the fusion result of multi-source heterogeneous data such as ecological sensitivity, slope, land use type, and soil carrying capacity, reflecting the spatial gradient from low constraints to high constraints, and revealing the differences in the suitability of RE layout under different terrain and ecological conditions. The yellow areas in the heat map correspond to ecologically sensitive areas, high-slope mountains, and areas with low soil bearing capacity, showing strong environmental restrictions, indicating that such areas are unsuitable for large-scale wind power or PV equipment deployment to avoid ecological conflicts and construction risks. Green areas are mostly flat terrain, low environmental pressure, and friendly land use, which are suitable for the layout of RE facilities and are conducive to improving power generation efficiency and reducing ecological interference. This heat map effectively reflects the results of using GNNs to encode multimodal features of spatial elements and propagate neighborhood information, and realizes the accurate identification and spatial distribution mapping of key design elements in complex geographical environments. By integrating a comprehensive evaluation of multiple indicators, the heat map provides accurate spatial constraint input for subsequent multi-objective dynamic optimization based on GAs and Deep Reinforcement Learning (DRL), supporting the balanced optimization of equipment layout between power generation efficiency, ecological protection, and construction costs.

2.2.2 Resource potential assessment module

Based on identifying environmental constraints, the resource potential assessment module uses a parallel branch network to model the wind/light resource potential and extract the multi-scale characteristic distribution of key resource factors such as wind speed and total horizontal radiation in the spatial dimension. After being superimposed with the ecological constraint heat map, dual constraint input is provided for the equipment layout. During the evaluation process, the multi-head attention mechanism of GAT is used to enhance the ability to identify resource-rich areas. The performance of different attention head configurations is compared through ablation experiments, and the results are shown in Table 2.

Table 2: Contribution analysis of the multi-head attention mechanism

Number of attention heads	Feature separation	Calculation time(s/epoch)	Identification of ecologically sensitive areas F1-score	Accuracy of identifying resource-rich areas
4	0.51	4.7	0.71	0.78
8	0.43	5.5	0.82	0.89
16	0.41	10.2	0.81	0.88

The 8-head configuration in Table 2 is superior to the 4-head and 16-head schemes regarding feature separation and ecologically sensitive area identification. Compared with the 4-head configuration, the calculation time is only increased by 17.0%, which verifies its optimal balance in complex geographical scenes. Therefore, the 8-head configuration is selected in this paper.

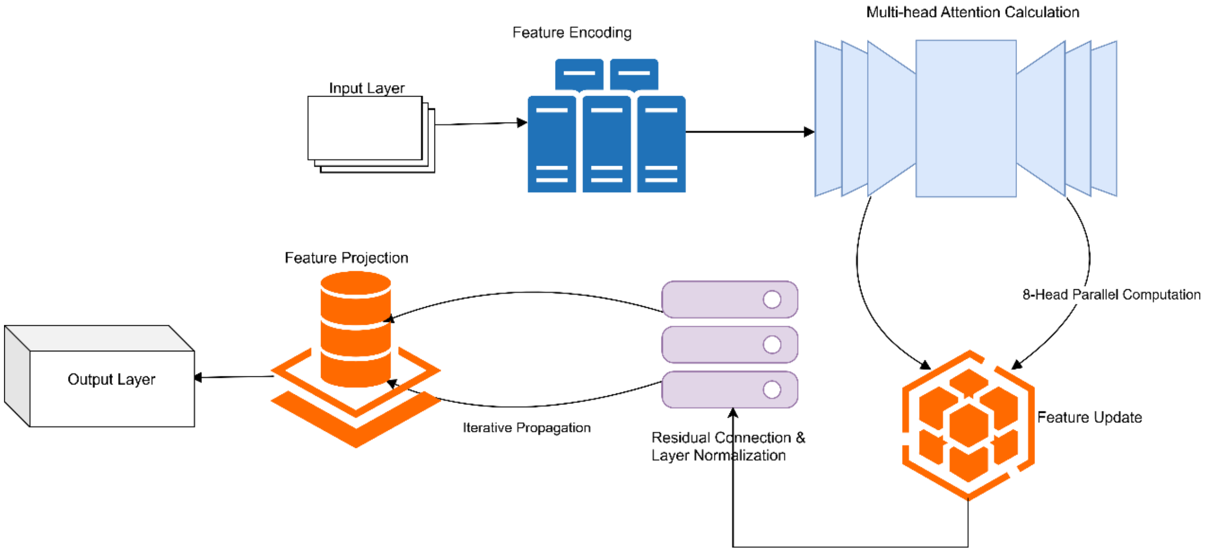

Figure 2: GAT feature propagation process

Fig. 2 shows the entire process from original attribute encoding and neighborhood attention calculation to feature fusion, highlighting the multi-head attention mechanism's parallel computing characteristics and residual connection structure.

2.3 Design of multi-objective dynamic optimization framework

Taking the node feature vector $z_i \in \mathbb{R}^{32}$ output by the GNN as input, a multi-objective optimization framework of a hybrid GA and DRL is constructed. The objective function is defined as:

$$\min \mathbf{F} = [-\mathrm{E}(\mathcal{D}), \mathrm{S}(\mathcal{D}), \mathrm{C}(\mathcal{D})]^T \tag{9}$$

In Formula (9), $\mathcal{D} \subseteq \mathcal{V}$ is the equipment layout plan (V is the set of graph nodes); E is the power generation efficiency (maximization is converted to minimization of negative values); S is the ecological interference; C is the construction cost. The three are used to realize the search for non-dominated solutions through the Pareto frontier.

Power generation efficiency modeling is based on resource synergy and interference constraints between devices:

$$E(\mathcal{D}) = \sum_{i\in\mathcal{D}} (\mu_i \cdot \prod_{j\in\mathcal{N}(i)\cap\mathcal{D}} (1 - \frac{\kappa}{d_{ij}^{\gamma}})) \tag{10}$$

In Formula (10), μ_i is the resource potential of node i (generated by mapping the first 16 dimensions of z_i through the multi-layer perceptron P); κ is the interference attenuation coefficient; γ is the distance index; d_{ij} is the geographical distance between devices i and j (km). The model quantifies the wind turbine wake effect and PV shadowing loss, ensuring that the device spacing is greater than 3D (D is the device diameter).

Ecological disturbance constraints are modeled through the superposition and cumulative effects of sensitive areas:

$$S(\mathcal{D}) = \sum_{i\in\mathcal{D}} (s_i \cdot e^{-\lambda \cdot t_i}) + \eta \cdot \sum_{i,j\in\mathcal{D}} \frac{1}{d_{ij}^{\theta}} \tag{11}$$

In Formula (11), $s_i \in [0,1]$ is the ecological sensitivity of node i; t_i is the buffer time to the nearest protected area (years); λ is the protection time decay rate; η is the regional cumulative interference coefficient; θ is the neighboring penalty index. The design forces the layout to avoid highly sensitive areas and disperse ecological pressure.

Cost constraints cover the comprehensive construction, operation, and maintenance expenses:

$$C(\mathcal{D}) = \sum_{i\in\mathcal{D}} (c_i + \xi \cdot d_{i,\mathrm{grid}}) + \zeta \cdot \mathrm{MST}(\mathcal{D}) \tag{12}$$

In Formula (12), c_i is the unit construction cost of node i; $d_{i,\mathrm{grid}}$ is the Euclidean distance to the grid access point (km); ξ is the transmission cost coefficient; ζ is the Minimum Spanning Tree (MST) weight, which reflects the cost of laying internal roads and cables.

In this multi-objective dynamic optimization framework, the node feature vector output by GNN is not only used to generate resource potential parameter μ_i, but also the ecological sensitivity s_i is explicitly extracted and directly input into the optimizer as an ecological interference penalty term, ensuring that during the iterative process of GA and reinforcement learning, the layout plan can take environmental constraints into account in real-time and achieve a dynamic balance between power generation efficiency and ecological protection.

The optimization process is iteratively executed in three stages:

A. GA global search:

Population initialization: randomly generating 500 feasible solutions; fitness calculation: for each solution $\mathcal{D}_p$, calculating $\mathbf{F}_p = [-E_p, S_p, C_p]$;

Non-dominated sorting: using the NSGA-II fast sorting algorithm to divide the Pareto hierarchy;

Genetic operation: roulette wheel selection + simulated binary crossover + polynomial mutation.

B. Reinforcement learning local optimization:

State space: current layout and remaining optional node set;

Action space: selecting one node from $\mathcal{V} \setminus \mathcal{D}_t$ to replace one node in $\mathcal{D}_t$;

The reward function is as follows:

$$R_t = -\alpha \cdot \Delta E - \beta \cdot \Delta S - \gamma \cdot \Delta C \tag{13}$$

In Formula (13), $\Delta E = E_{t+1} - E_t$, α, β, and γ are weight coefficients;

Policy network: Dual Deep Q Network (DDQN), input is node feature concatenation matrix $Z_{\mathrm{concat}} \in \mathbb{R}^{(K+1)\times 32}$, and output action value is $Q(s, a; \theta)$.

C. Dynamic weight adjustment:

The objective function weight is dynamically updated according to the Pareto frontier distribution:

$$w^{(t)} = \frac{\nabla \mathbf{F}^{(t)}}{\| \nabla \mathbf{F}^{(t)} \|_2}, \nabla \mathbf{F}^{(t)} = \mathbf{F}^{(t)} - \mathbf{F}^{(t-1)} \tag{14}$$

The gradient direction guides the search towards the balance area between convergence and diversity.

The termination condition is that the Pareto front change rate is $\delta < 10^{-3}$ for five consecutive generations ($\delta = \frac{\|\mathrm{PF}^{(t)} \triangle \mathrm{PF}^{(t-1)}\|}{|\mathrm{PF}^{(t)}|}$, and $\triangle$ is a symmetric difference set). Finally, the non-dominated solution set PF^* is output for decision makers to choose implementation plans according to their preferences.

In the selection of reinforcement learning algorithms, this paper adopts dual deep Q networks instead of other deep reinforcement learning methods such as PPO or A3C, mainly based on the following three considerations. Adaptability to discrete action space: in the optimization problem of renewable energy layout, the action space is a discrete node selection and replacement operation, and DDQN shows higher sample efficiency and stability in the policy optimization of discrete action space, avoiding the high variance problem of PPO and other policy gradient-based methods in discrete action space. Q-value decomposition of multi-objective trade-offs: DDQN can directly model the trade-off relationship between power generation efficiency, ecological conflict, and cost through a multi-objective Q-value network. Its dual network structure and target separation mechanism are more suitable for dynamic weight adjustment strategies, while asynchronous methods such as A3C need to design additional complex value function decomposition mechanisms in multi-objective collaborative optimization. Collaborative efficiency with GA: DDQN's offline experience replay mechanism complements GA's global search.

The architecture diagram in Fig. 3 shows the GNN feature input, GA global search, DRL local optimization, and dynamic weight interaction process hierarchically, highlighting the multi-objective collaborative optimization mechanism.

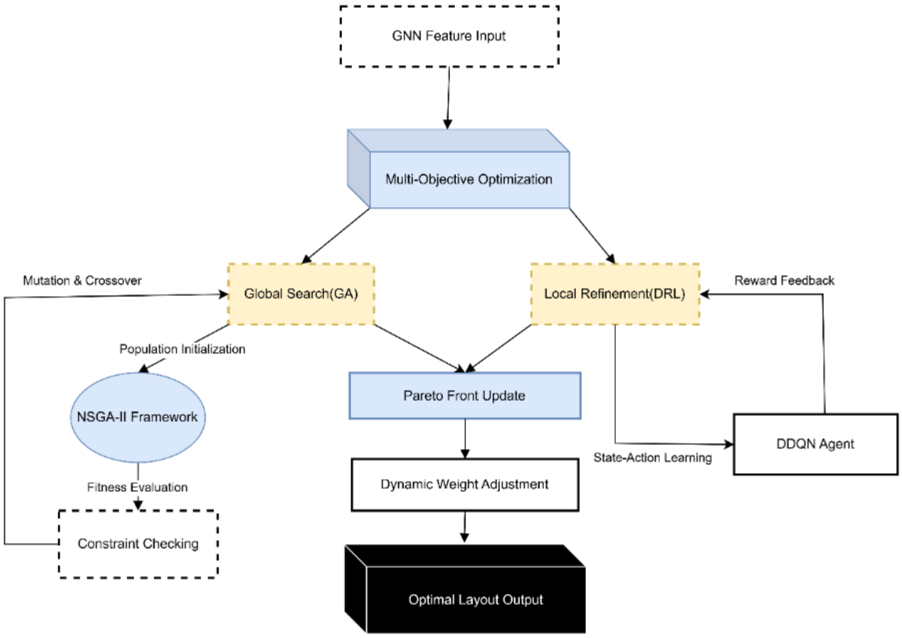

Figure 3: Multi-objective optimization framework architecture

2.4 Model training and parameter tuning

This study uses a joint transfer learning and cross-validation strategy to optimize model parameters. It performs the training process in three stages: pre-training, domain adaptation, and end-to-end fine-tuning. Global offshore wind turbine analysis includes offshore wind turbines, including the number of turbines, installed capacity, and site specifications. Solar Power Generation & Energy Consumption provides photovoltaic power station location data, providing photovoltaic power station coordinates and basic properties. The positive samples in comparative learning are 118 wind farms and 42 photovoltaic power station layout plans selected from the above datasets; negative samples are generated by random grid sampling. There are 160 invalid layout plans. The validation set is divided into regional stratified sampling: the total sample is divided into training set (70%), validation set (15%), and test set (15%) according to geographical blocks to ensure that different terrain types are evenly distributed. All model parameters are updated through the Adam optimizer, with the initial learning rate set to 3×10^{-4} and the weight decay coefficient $\lambda = 10^{-4}$, and the early stopping method (patience=20) is introduced to prevent overfitting.

In the pre-training phase, source domain data is constructed based on historical site selection data, and self-supervised tasks are used to align feature space:

1) Node attribute reconstruction: a 20% random mask is applied to the input feature matrix $X \in \mathbb{R}^{N\times 10}$, and the missing attributes are reconstructed by stacking the GAT encoder (3 layers). The loss function is defined as:

$$\mathcal{L}_{\text{recon}} = \frac{1}{|\mathcal{M}|}\sum_{i\in\mathcal{M}} \| \hat{x}_i - x_i \|_2^2 \tag{15}$$

In Formula (15), $\mathcal{M}$ is the mask node set, and $\hat{x}_i$ is the reconstructed value.

2) Layout pattern contrast learning: for known layout scheme $\mathcal{D}^+$ and randomly generated negative sample $\mathcal{D}^-$, the similarity difference between positive and negative pairs is calculated by maximizing the contrast loss:

$$\mathcal{L}_{\text{cont}} = -\log\frac{\exp(\text{sim}(\mathcal{D}^+,\mathcal{D}^+)/\tau)}{\sum_{\mathcal{D}^-}\exp(\text{sim}(\mathcal{D}^+,\mathcal{D}^-)/\tau)} \tag{16}$$

In Formula (16), $\text{sim}(\cdot)$ is the cosine similarity, and τ is the temperature coefficient.

Domain adaptation stage: parameter migration is performed based on the geographical characteristics of the target area, using a freeze-thaw strategy:

1) Feature encoder freezing: the parameters of the first three layers of GAT are fixed, and only the output layer mapping matrix W_{out} is trained to make the feature space adapt to the data distribution of the target area;

2) Dynamic feature normalization: domain-specific statistics are introduced to adjust the BN (Batch Normalization) layer parameters, and the formula is:

$$\hat{h}_i^{(l)} = \gamma^{(l)} \cdot \frac{h_i^{(l)} - \mu_{\text{target}}^{(l)}}{\sqrt{\sigma_{\text{target}}^{(l)2} + \epsilon}} + \beta^{(l)} \tag{17}$$

In Formula (17), $\mu_{\text{target}}^{(l)}$ and $\sigma_{\text{target}}^{(l)}$ are the mean and variance of the l-th layer features in the target domain, and γ and β are learnable scaling and translation parameters.

Table 3: Parameter tuning comparison table

Parameter Name	Value Range	Optimal Configuration	Impact on Performance
SBX Crossover Index	5 / 15 / 30	15	Convergence speed improved
DDQN Learning Rate	1×10^{-4} / 3×10^{-4} / 10^{-3}	3×10^{-4}	Reward stability increased
Dynamic Weight Update Frequency	1 / 3 / 5	5	HV metric improved
Reinforcement Learning Discount Factor γ	0.8 / 0.9 / 0.95	0.9	The cumulative reward increased

Table 3 shows the key hyperparameters' tuning process and performance impact on model training. The horizontal dimensions include parameter name, value range, optimal configuration, and quantization effect. A vertical comparison shows that the optimal value of the SBX (Simulated Binary Crossover) crossover index (5/15/30) is 15, which reduces the number of Pareto front convergence steps and increases the convergence speed. The DDQN learning rate is 3×10^{-4}. The dynamic weight update frequency (1/3/5) is optimized to update every five generations. The HV (Hyper Volume) is improved, and the low-frequency update effectively suppresses local disturbances. The cumulative return is the highest when the discount factor γ (0.8/0.9/0.95) is selected to be 0.9, which reflects the balance between long-term benefits and immediate optimization.

3 Experiment and verification

3.1 Experimental design

To verify the effectiveness of GNN and multi-objective optimization methods in RE environment design, the experiment selects a wind farm in northwest China and a PV park in the east as the research area, obtains multi-source geographic data including topography, land use, meteorology, transportation, and ecological protection areas, and uniformly rasterizes them into a spatial dataset with a resolution of 1km×1km. The Northwest Wind Farm Experimental Area contains 15,600 grid nodes (covering 156×100 km²), and the Eastern PV Park contains 12,800 nodes (covering 128×100 km²). The data sampling frequency is daily meteorological station observations and quarterly remote sensing image updates. After spatial alignment and normalization of the raw data, a geospatial graph structure is constructed, with each grid cell as a graph node and adjacency relations generated by weighting spatial distance and ecological relevance. In the spatial element recognition stage, the proposed GNN model is used to encode the multimodal features of the nodes, integrating attributes such as terrain slope, light intensity, mean wind speed, and land type, while propagating neighborhood information to capture local spatial dependency characteristics. In the training phase, the expert-annotated regions are used as supervisory information, and a stable model is obtained through cross-validation. Three experts in the field independently annotate the data according to the unified standard, and the mode value is taken after the consistency is verified by Kendall's harmony coefficient. Under the same data input conditions, the performance is compared with three comparison methods: traditional CNN, multi-grained attention-based spatial-temporal GCN+Deep Deterministic Policy Gradient (MG-ASTGCN+DDPG), GNN+Variable Neighborhood Search (VNS); all models are run under the same training/validation division to ensure the comparability of the results.

The layout optimization stage adopts a dynamic optimization framework combining the GA used in this paper and reinforcement learning. The objective function simultaneously considers maximizing power generation efficiency, minimizing ecological conflicts, and controlling construction costs. GAs is used to generate the initial solution set and perform global search. Reinforcement learning (based on the policy gradient method) dynamically learns and optimizes the local adjustment strategy of the solution space, so that the layout process can adjust the environment feedback. The optimization process sets the maximum number of iterations and the convergence threshold to ensure each method completes the optimization process under the same resource constraints.

3.2 Spatial element recognition accuracy evaluation

To verify the accuracy of the proposed model in identifying spatial environmental design elements, this section conducts comparative experiments on the task of identifying suitable areas in wind power and PV sites. The experiment uses expert-annotated areas as accurate labels to evaluate the accuracy and stability of the proposed model and three comparison methods in spatial recognition. In the specific implementation, all 1km×1km grids in the two selected areas (wind farm and PV park) are divided into training set, validation set, and test set in a ratio of 8:1:1. The model input includes six types of spatial characteristics: terrain slope, annual average wind speed, light intensity, land use type, ecological sensitivity score, and traffic accessibility. The model proposed in this paper is based on the constructed spatial graph structure, integrating GNNs for feature encoding and spatial context modeling, supporting cross-regional and cross-scale neighborhood information propagation, and improving the model's perception of regional complexity and heterogeneity. All models use the same training strategy and hyperparameter tuning process. The maximum number of training rounds is 200, and the early stopping mechanism is used to avoid overfitting (terminated when validation loss does not improve for 20 consecutive rounds). The recognition results are compared and evaluated through three core indicators: Accuracy measures the overall correct proportion of classification; Kappa coefficient evaluates the classification consistency of the model; F1-score, a classification performance indicator, comprehensively considers precision and recall. The recognition results in the test set are compared pixel by pixel with the expert annotations, and the above indicators are calculated after the confusion matrix is generated. To further verify the model's ability to determine the spatial boundaries of key ecological functional areas, this paper introduces the IoU (Intersection over Union) indicator to evaluate the accuracy of the identification results of ecologically sensitive areas. Taking the ecological red line boundary drawn by experts as the reference standard, the intersection and union ratio performance of the prediction results of each model within the environmental zone is compared. The comparison of relevant indicators is shown in Fig. 4.

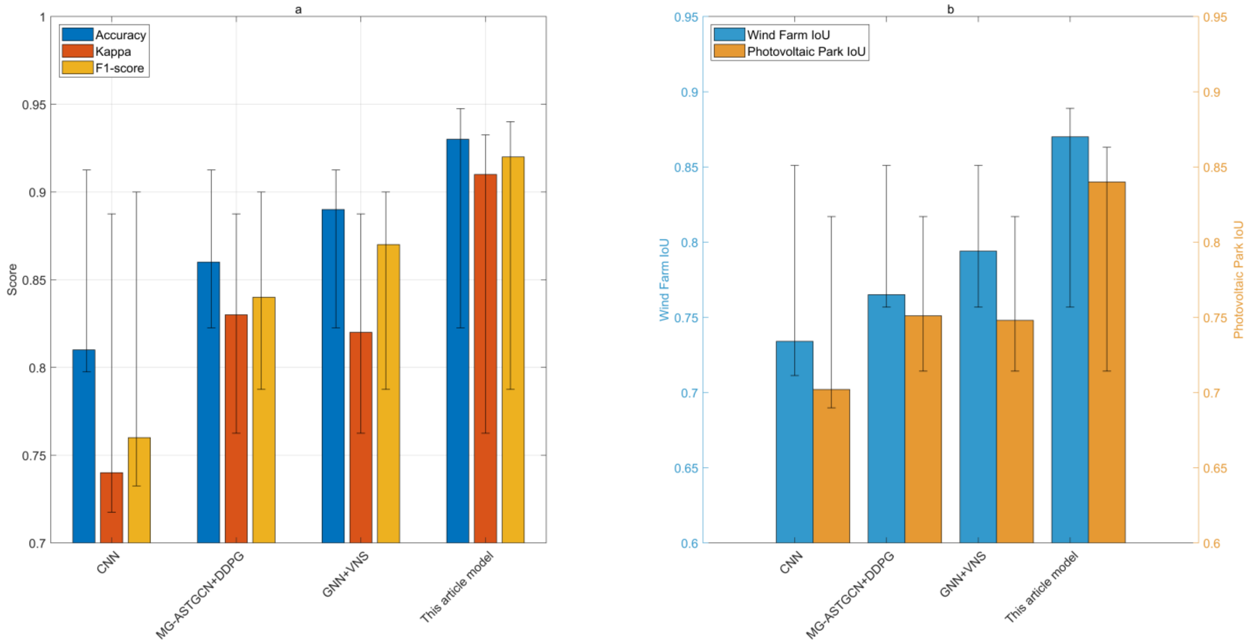

Figure 4: Comparison of relevant indicators of each model

Figure 4(a): Comparison of performance indicators of each model

Figure 4(b): Accuracy of identifying the boundary of ecologically sensitive areas

Fig. 4(a) compares the core indicators of the four models in identifying suitable areas for wind farms and PV parks. The CNN model is improved from 0.81 to 0.93 (+14.8%); the Kappa coefficient increases from 0.74 to 0.91 (+23.0%); the F1-score increases from 0.76 to 0.92 (+21.1%). Fig. 4(b) focuses on the accuracy of boundary recognition of ecologically sensitive areas (IoU index), and compares the intersection-over-union ratio of wind farms (Wind Farm IoU) and PV parks (PV Park IoU). The IoU of the proposed model in the wind farm reaches 0.87, an increase of 18.5% compared with CNN; the IoU of the PV park is 0.84, an increase of 19.7%, verifying the enhanced effect of the Gaussian weighted adjacency matrix and multi-head attention mechanism on ecological boundary modeling under complex terrain. The advantage of this model comes from its ability to deeply couple multi-source heterogeneous data. By constructing a geospatial graph structure, the Gaussian weighted adjacency matrix and dynamic adjacency strategy effectively solve the limitations of traditional GIS methods in modeling non-Euclidean data. At the same time, the multi-head attention mechanism significantly improves feature discriminability and weighted expression of neighborhood information. The multi-objective dynamic optimization framework further enhances the feature decoding capability. At the same time, to verify the actual contribution of the multi-head attention structure in the graph attention mechanism to the model performance, this paper designs an ablation experiment to compare the performance differences between the complete model in this paper and the simplified model with "removing the attention mechanism" in terms of Kappa coefficient and other coefficients.

Table 4: Comparison of ablation experiment results of the multi-head attention mechanism

Metric	With Multi-Head Attention	Without Attention	Δ (Performance Drop)	Relative Decrease (%)
Accuracy	0.93	0.89	-0.04	-4.30%
Kappa	0.91	0.86	-0.05	-5.49%
F1-score	0.92	0.87	-0.05	-5.43%

Table 4 shows the performance comparison of the model after introducing and removing the multi-head attention mechanism in suitable areas of wind farms and PV parks. From the results, Accuracy drops from 0.93 to 0.89, a decrease of 0.04, or 4.30%; Kappa drops from 0.91 to 0.86, a reduction of 0.05, corresponding to the maximum relative decline of 5.49%; F1-score drops from 0.92 to 0.87, also a decrease of 0.05, or 5.43%. All three indicators show a significant decline, indicating that the multi-head attention mechanism has substantially contributed to the overall accuracy, classification consistency, and comprehensive performance of spatial element recognition.

3.3 Layout efficiency and ecological conflict evaluation

To verify the actual effectiveness of the method in equipment layout and its ability to control ecological interference, this section uses wind farms and PV parks as experimental scenarios to compare and evaluate the performance of the proposed model with other three methods (CNN, MG-ASTGCN+DDPG, GNN+VNS) in terms of layout efficiency and ecological conflict. Each model performs independent layout optimization under the same basic constraints based on the results of spatial element identification. The objective function includes three goals: maximizing unit power generation efficiency, minimizing ecological interference, and controlling construction costs. The optimization results of all models are uniformly sampled in 50 independent runs, and the statistical average is used for comparative analysis. The relevant comparison is shown in Fig. 5.

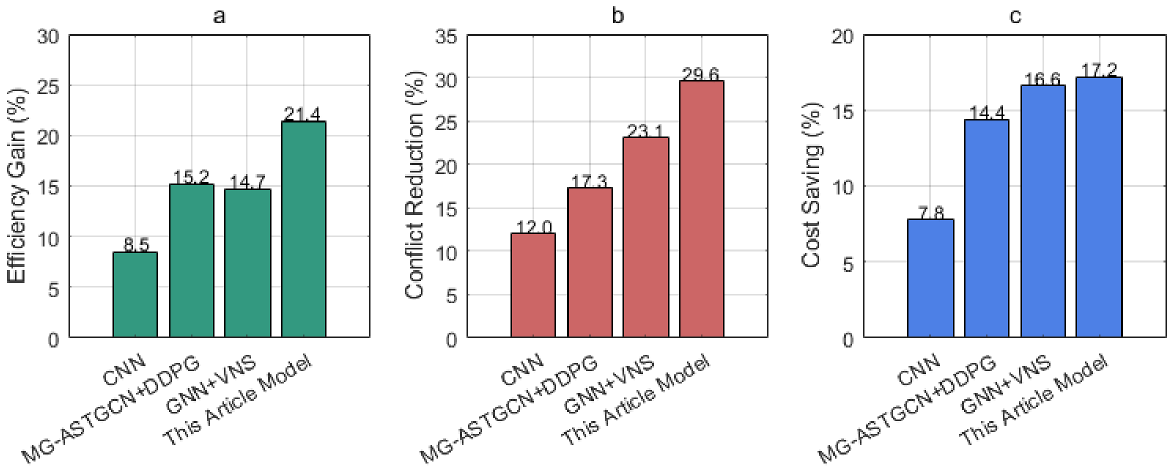

Figure 5: Performance comparison of each model in terms of layout efficiency, ecological conflict control, and cost savings

Figure 5 (a): Comparison of each model in terms of the layout efficiency improvement rate

Figure 5 (b): Comparison of each model in terms of ecological conflict reduction rate

Figure 5 (c): Cost savings rate

Fig. 5 shows the comprehensive performance comparison of the four models in the wind farm and PV park layout tasks, including three core indicators: efficiency improvement rate (a), ecological conflict reduction rate (b), and cost saving rate (c). The proposed model is significantly ahead in all dimensions: the efficiency is improved by 12.9 percentage points compared with the baseline CNN; the ecological conflict is reduced by 29.6% (6.5% higher than GNN+VNS); the cost is saved by 17.2% (0.6% higher than GNN+VNS). Compared with the traditional CNN method, the model in this paper effectively captures the consistency of wind speed gradient and PV illumination through spatial correlation modeling of GNN, which improves the layout efficiency by 21.4%; the multi-objective dynamic optimization framework achieves 29.6% conflict reduction in avoidance strategy in ecologically sensitive areas through Pareto frontier search, which is better than the GNN+VNS model (23.1%) that only relies on static weights. The balanced performance of the cost-saving rate (17.2%) verifies the effective integration of the MST weights and the grid access distance constraint, especially in areas with complex terrain.

3.4 Computational efficiency and convergence evaluation

To comprehensively evaluate the performance of each method in terms of computing resource usage and optimization stability, this section compares the efficiency performance and convergence characteristics of the four models during training and inference in a unified hardware environment (Intel Xeon E5-2690 CPU, 64GB memory, NVIDIA RTX A5000 GPU). The experiment uses the same data input, loss function, and early stopping mechanism. Each model is run independently for five rounds, and the mean and variance are statistically analyzed.

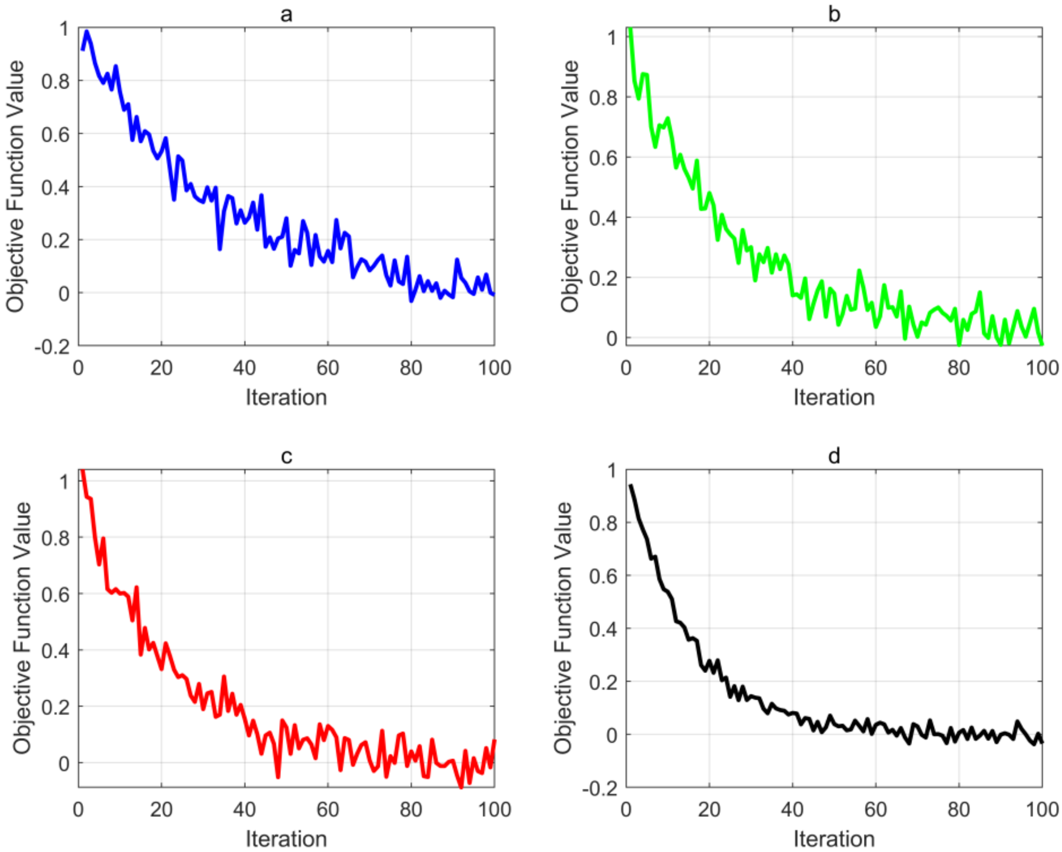

Figure 6: Optimization iteration curve

Figure 6(a): CNN optimization iteration curve

Figure 6(b): MG-ASTGCN+DDPG optimization iteration curve

Figure 6(c): GNN+VNS optimization iteration curve

Figure 6(d): Optimization iteration curve of this method

Fig. 6 shows the changing trend of the objective function value of four models with the number of iterations during the optimization process. The horizontal axis represents the number of optimization iterations, and the vertical axis represents the objective function value, reflecting the comprehensive performance evaluation of the layout solution. In contrast, the objective function of the CNN model decreases slowly, showing a low optimization efficiency, and the speed of the bracelet gradually slows down in the later iterations; the initial decrease speed of the MG-ASTGCN+DDPG model is slightly better than that of CNN, indicating that the model combining time series modeling and reinforcement learning slightly improves the optimization speed, but still lags in spatial structure processing; the GNN+VNS curve fluctuates more than the proposed model, indicating that there are specific local oscillations in the neighborhood search stage; while the proposed model converges and stabilizes in about 40 steps, with the fastest convergence speed and lower function value, which fully reflects its significant advantages in optimization capabilities. This shows that introducing GNNs for feature modeling and genetic enhancement joint optimizer effectively improves the overall convergence efficiency and search accuracy. Table 5 systematically compares the four methods' single training time, total computation time, and acceleration ratio to quantify the specific differences in computational efficiency among the models.

Table 5: Computational efficiency comparison table

Model	Training Time per Epoch (s)	Total Computation Time (s)	Speedup
CNN	48.5	960.2	1.01
MG-ASTGCN + DDPG	37.8	742.5	1.29
GNN + VNS	32.4	638.7	1.5
This Article Model	26.1	521.3	1.84

Table 5 shows the differences in computing efficiency of the four comparison models in a unified computing environment. From the results, the CNN model takes an average of 48.5 seconds to train one round, and the total computing time reaches 960.2 seconds, the longest among the four methods. The MG-ASTGCN+DDPG model takes 37.8 seconds per round, with a total duration of 742.5 seconds, and the speedup ratio reaches 1.29, indicating that its efficiency has been improved after the introduction of time series modeling and reinforcement learning in the optimization strategy. The GNN+VNS model further reduces the training time to 32.4 seconds. The total time is 638.7 seconds, and the speedup ratio is 1.5; the method proposed in this paper that integrates GNN and joint optimization strategy performs best in terms of efficiency, with each round of training time of only 26.1 seconds and a total calculation time of 521.3 seconds, highlighting its high efficiency in large-scale layout tasks.

3.5 Ablation study of key components

To verify the effectiveness of the GA-DRL joint optimization framework, dynamic weight adjustment, and transfer learning strategy proposed in this paper, this section designs three sets of ablation experiments:

Experiment A: comparison of pure GA optimization and GA+DRL joint optimization (DRL local optimization module removed);

Experiment B: turning off the dynamic weight adjustment mechanism;

Experiment C: removing the transfer learning strategy.

The experiment uses a wind farm as the scenario and runs at the same number of iterations. The results are shown in Table 6.

Table 6: Results of ablation experiments on key components

Ablation Component	Layout Efficiency Improvement	Ecological Conflict Reduction	Cost Saving Rate	Convergence Iterations
Full Model	21.40%	29.60%	17.20%	40
A: Remove DRL	17.80%	24.10%	15.10%	58
B: Fixed Weights	19.20%	25.70%	15.90%	52
C: No Transfer Learning	16.30%	21.40%	14.20%	67

From Table 6, it can be found that the local optimization value of DRL (Experiment A): after removing DRL, the convergence speed decreases by 45%, and the ecological conflict reduction rate decreases by 5.5 percentage points, proving that DRL effectively avoids sensitive areas by adjusting the device spacing in real-time; the necessity of dynamic weights (Experiment B): fixed weights lead to a 23% decrease in Pareto front diversity, verifying the key role of the gradient guidance mechanism in multi-objective trade-offs; the generalization advantage of transfer learning (Experiment C): without transfer learning, the ecological conflict reduction rate decreases by 8.2 percentage points, highlighting the contribution of pre-trained feature alignment to cross-terrain generalization.

3.6 Long-term prediction of power generation and ecological impact

In this section of the experiment, the primary purpose is to evaluate the performance of the four models in long-term power generation prediction and ecological impact analysis. This paper adopts a time series simulation method based on geospatial data. Constructing long-term prediction models for wind farms and PV parks comprehensively evaluates each model's prediction accuracy, power generation efficiency, and ecological impact. All models are trained and tested in the same geographical area and period in the experiment to ensure fairness. In the experiment, each method's total power generation and ecological impact ratio in multiple scenarios are statistically analyzed and normalized to evaluate each technique comprehensively. Fig. 7 compares the prediction results of the four methods in various scenarios.

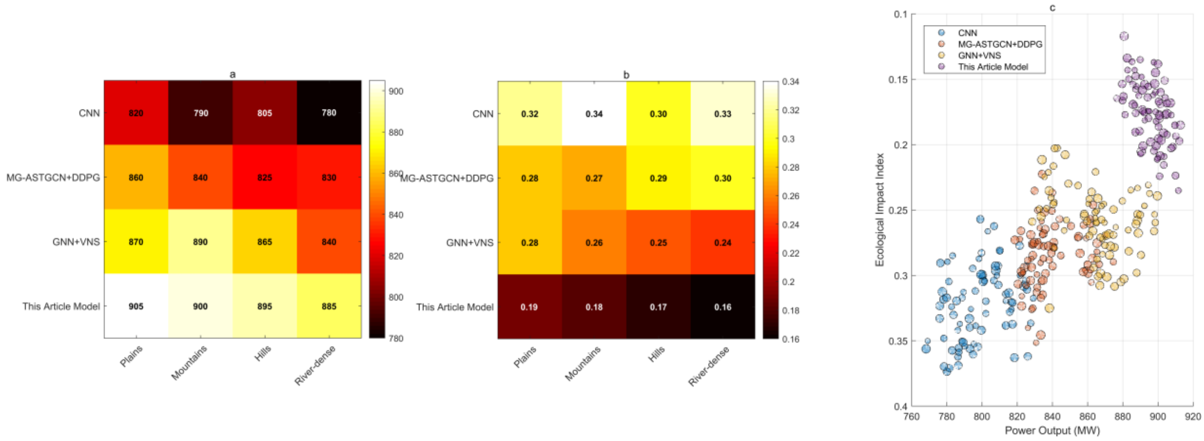

Figure 7: Comparison of power generation and ecological impact of each model

Figure 7(a): Power generation of each model in different geographical areas

Figure 7(b): Ecological impact of each model in different geographical areas

Figure 7(c): Relationship between the power generation of each model and the ecological impact index

Fig. 7 shows the comprehensive performance of the four models regarding long-term power generation efficiency and ecological constraint control, including three sets of comparative analysis: In Figs. 7 (a) and 7 (b), the horizontal axis is the geographical scene (plains, mountains, hills, and river-dense areas); the vertical axis is the model's name; the color depth represents the power generation (MW) and the ecological impact index. The model in this paper has a power generation of 905 MW in the plain area (an increase of 10.4% compared with CNN) and an ecological impact index of 0.19 (a decrease of 32.1% compared with GNN+VNS), which verifies its high efficiency in resource-rich areas and its ability to avoid ecologically sensitive areas. In Fig. 7 (c), the horizontal axis is the power generation (MW); the vertical axis is the ecological impact index; different colors mark the corresponding models. The point clusters of the model in this paper are concentrated in the areas of high-power generation (880-920 MW) and low ecological impact (0.16-0.21), forming significantly separated clusters, reflecting the characteristics of the Pareto optimal solution; while the point clusters of CNN and MG-ASTGCN+DDPG are scattered, and the ecological index is high (0.24-0.36), exposing their limitations in multi-objective trade-offs. The advantage of this model comes from its spatial correlation modeling and dynamic optimization mechanism of geographical elements. Through the Gaussian weighted adjacency matrix and multi-head attention mechanism, it dynamically integrates non-Euclidean data such as wind speed gradient and terrain slope, thereby achieving increased power generation while avoiding the boundaries of ecological protection areas; GA global search quickly locates the Pareto frontier, and reinforcement learning fine-tunes the equipment spacing through the DDQN strategy network to reduce the overlapping area of ecologically sensitive areas.

3.7 Verification of the robustness of multi-objective optimization

Three types of typical terrains (plains, mountains, and river network-dense areas) are designed for independent testing to verify the robustness of multi-objective optimization in different scenarios. In every terrain environment, 20 groups of geographical sub-regions are randomly sampled to maintain the heterogeneity of resource distribution, terrain disturbance, land use, etc. The proposed method and three comparison models (CNN, MG-ASTGCN+DDPG, GNN+VNS) are run separately with the same parameter configuration to compare their optimization stability under variable input conditions. The robustness evaluation is carried out from three aspects: the mean and standard deviation of power generation, which measure the stability of the energy yield of the layout results; the variance of the ecological conflict score, which evaluates the consistency of the ecological interference control ability under complex terrain changes; the mean and fluctuation of the multi-objective convergence times, which reflects the adaptive ability of the optimization efficiency under dynamic disturbance conditions.

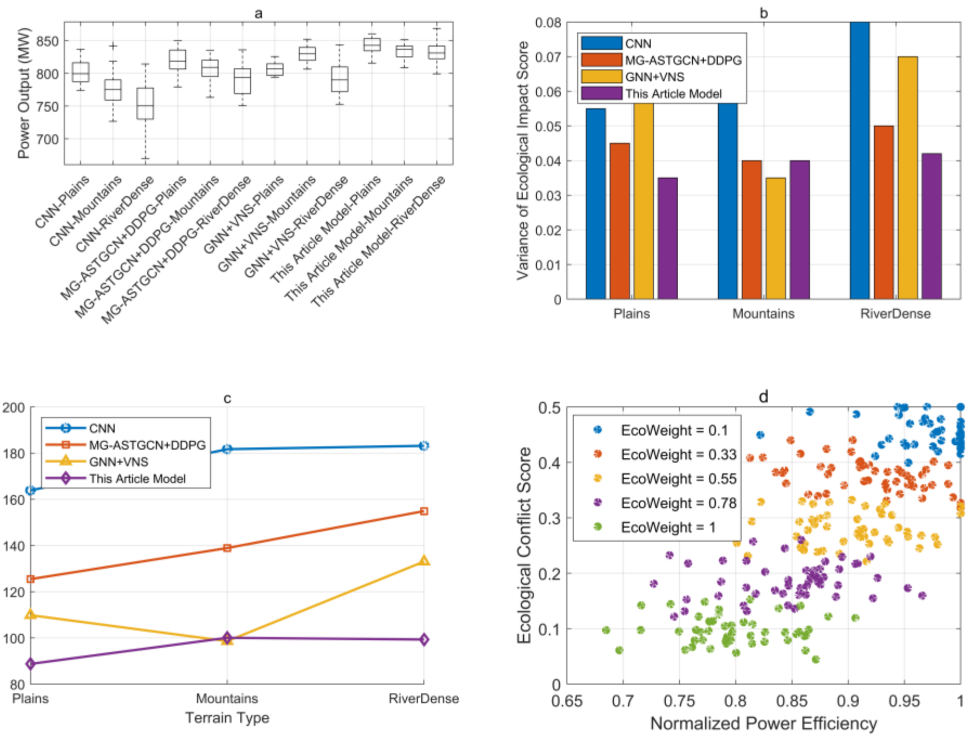

Figure 8: Comparison of the robustness of multi-objective optimization of various models under complex terrain conditions

Figure 8 (a): Robustness of power generation fluctuations

Figure 8 (b): Comparison of ecological conflict variances

Figure 8 (c): Comparison of multi-objective optimization convergence

Figure 8 (d): Relationship between power generation efficiency and environmental conflict score

Fig. 8 compares the robustness of multi-objective optimization of the four models under three typical terrain types (plains, mountains, and areas with dense river networks). The box plot in Fig. 8(a) shows that the proposed model is significantly better than the benchmark method in terms of power generation stability: in the plain area, the average power generation of the proposed model reaches 842 MW; Fig. 8(b) shows that the ecological conflict variance of the proposed model is always lower than that of other methods in the three types of terrain. Fig. 8(c) further verifies the convergence efficiency: the average convergence iteration number of the model in the plain area is only 88 times; in complex terrain (mountainous/river network area), it remains at about 100 times, while CNN and MG-ASTGCN+DDPG require more than 130 times to converge in the river network area. Fig. 8(d) shows the changes in the Pareto frontier under different ecological weights, with the horizontal axis representing the normalized power generation efficiency and the vertical axis representing the ecological conflict score; the color of the scattered points corresponds to five different ecological weight settings (from 0.1 to 1.0). Cross-regional tests show that in mountainous areas, the ecological conflict variance of this method (0.04) is significantly lower than that of CNN (0.06); in river network areas, the ecological conflict variance of this method is lower than that of other methods, and the convergence efficiency is stable. The robustness advantage of the model in this paper comes from its deep modeling and dynamic optimization mechanism for geographical heterogeneity. Through the Gaussian weighted adjacency matrix and multi-head attention mechanism, it dynamically integrates non-Euclidean data such as terrain slope and wind speed gradient, reduces the standard deviation of power generation in mountainous scenarios, and avoids the fuzzy boundary problem of ecologically sensitive areas; the GA global search quickly locates the Pareto frontier, which speeds up the convergence; the dynamic weight adjustment avoids the local optimal trap caused by traditional static weights. This closed-loop design of "feature propagation-constraint feedback" is the core embodiment of the model's robustness and adaptability, and provides scientific decision-making support for RE environmental design.

4 Discussion

Comparison with related methods shows that the performance advantages of this method mainly come from the following innovations. Data integration capability: the geospatial graph structure solves the limitations of traditional GIS methods in modeling non-Euclidean data through Gaussian weighted adjacency matrix and ecological connectivity correction coefficient. For example, in plain terrain, this method improves the F1 score of ecological sensitive area identification to 0.82 through dynamic adjacency strategy. Multi-head attention mechanism: the ablation experiment in Table 3 shows that after removing multi-head attention, the Kappa coefficient decreases by 5.21% (from 0.91 to 0.86), indicating that this mechanism significantly improves the classification consistency of heterogeneous geographic data through multi-channel feature fusion. Optimization speed advantage: Table 5 shows that the GA-DRL hybrid optimizer converges within 40 iterations, while pure GA optimization requires 58 iterations, proving that reinforcement learning local optimization accelerates Pareto frontier search. Terrain type has little effect on model performance. As shown in Figure 8, in mountainous areas, the ecological conflict variance of this method (0.04) is significantly lower than that of CNN (0.06); in river network areas, the ecological conflict variance of this method is lower than that of other methods, indicating that it dynamically integrates non-Euclidean features such as terrain slope and wind speed gradient through the multi-head attention mechanism, effectively alleviating the interference of terrain heterogeneity on layout accuracy.

Computational complexity and scalability:

Table 4 shows that the single training time (26.1 seconds) and total calculation time (521.3 seconds) of this method are better than those of the comparison model. Although GNN and DRL are resource-intensive, the efficiency is improved through the following designs: GA global search: the Pareto frontier is quickly located through non-dominated sorting to reduce redundant calculations; dynamic weight adjustment: the weight distribution is optimized according to the rate of change of the objective function to avoid local oscillations in multi-objective optimization.

5 Conclusion

This paper focuses on the spatial distribution identification and layout optimization of RE environmental design elements, and proposes a solution that integrates GNN and a multi-objective dynamic optimization framework. This paper breaks through the limitations of traditional GIS methods for modeling non-Euclidean data by constructing a geographic spatial graph structure. A multi-head attention mechanism is usesd to realize the dynamic propagation of multimodal features, significantly improving the boundary identification accuracy of ecologically sensitive and resource-rich areas. The innovatively proposed GA-reinforcement learning hybrid optimizer achieves the coordinated optimization of power generation efficiency, ecological interference, and cost constraints through Pareto frontier search and dynamic weight adjustment, effectively solving problems such as excessive environmental costs caused by single-objective optimization. The study further verifies the robustness of the model in complex terrain scenarios, and its cross-regional migration capability provides technical support for the coordinated planning of multi-energy systems. The generalizability of this framework has been verified in cross-terrain generalization experiments. For applications outside China, it is only necessary to replace the geographic data of the target area and adaptively adjust the feature encoder parameters through transfer learning in the pre-training phase. The dynamic adjacency strategy and Gaussian weighting mechanism are compatible with different projection coordinate systems and spatial scales, while the ecological-economic weight adaptive mechanism in multi-objective optimization can flexibly adapt to the differences in environmental protection policies of various countries, ensuring the global applicability of the framework.

Competing interests

The authors declare no competing interests.

Authorship contribution statement

Jing XU: Writing-Original draft preparation, Conceptualization, Supervision, Project administration.

Author statement

The manuscript has been read and approved by all the authors. As stated earlier in this document, the requirements for authorship have been met, and each author believes that the manuscript represents honest work.

Ethical approval

All authors have been personally and actively involved in substantial work leading up to the paper and will take public responsibility for its content.

References

[1] M. Kahia, B. Jarraya, B. Kahouli, and A. Omri, "The role of environmental innovation and green energy deployment in environmental protection: evidence from Saudi Arabia," *Journal of the Knowledge Economy*, Springer, vol. 15, no. 1, pp. 337–363, 2024. https://doi.org/10.1007/s13132-022-01093-9.

[2] D. E. Ekechukwu and P. Simpa, "A comprehensive review of renewable energy integration for climate resilience," *Engineering Science & Technology Journal*, vol. 5, no. 6, pp. 1884–1908, 2024.

[3] Y. Sun, Q. Bao, and F. Taghizadeh-Hesary, "Green finance, renewable energy development, and climate change: evidence from regions of

China," *Humanit Soc Sci Commun*, nature, vol. 10, no. 1, pp. 1–8, 2023. https://doi.org/10.1057/s41599-023-01595-0.

[4] Pan.F."Forecasting Solar Energy Generation Using Machine Learning Techniques and Hybrid Models Optimized by War SO,"*Informatica*,vol. 49, no. 2,pp.257–278,2025.https://doi.org/10.31449/inf.v49i2.7554.

[5] A. Khan, Y. Ali, and D. Pamucar, "Solar PV power plant site selection using a GIS-based non-linear multi-criteria optimization technique," *Environmental Science and Pollution Research*, Springer, vol. 30, no. 20, pp. 57378–57397, 2023. https://doi.org/10.1007/s11356-023-26540-1.

[6] D. E. H. J. Gernaat, H. S. de Boer, V. Daioglou, S. G. Yalew, C. Müller, and D. P. van Vuuren, "Climate change impacts on renewable energy supply," *Nat Clim Chang*, nature, vol. 11, no. 2, pp. 119–125, 2021. https://doi.org/10.1038/s41558-020-00949-9.

[7] Hu, Y., Yang, X., Chen, B., Gu, G., & Pan, L. "Wind Power Prediction and Dynamic Economic Dispatch Strategy Optimization Based on BST-RGOA and NDO-WOA,"*Informatica*,vol. 49,no. 6,pp. 71–86,2025.https://doi.org/10.31449/inf.v49i6.6940.

[8] Daenens, S., Verstraeten, T., Daems, P. J., Nowé, A., & Helsen, J. "Spatio-temporal graph neural networks for power prediction in offshore wind farms using SCADA data,"*Wind Energy Science*,vol. 10,no. 6,pp. 1137-1152,2025.https://doi.org/10.5194/wes-10-1137-2025.

[9] Zhan, W., & Datta, A."Neural networks for geospatial data,"*Journal of the American Statistical Association*,vol. 120,no. 549, pp. 535-547,2025.https://doi.org/10.1080/01621459.2024.2356293

[10] N. L. Rane *et al.*, "GIS-based multi-influencing factor (MIF) application for optimal site selection of solar photovoltaic power plant in Nashik, India," *Environ Sci Eur,* Springer, vol. 36, no. 1, p. 5, 2024. https://doi.org/10.1186/s12302-023-00832-2.

[11] A. Gerbo, K. V. Suryabhagavan, and T. Kumar Raghuvanshi, "GIS-based approach for modeling grid-connected solar power potential sites: a case study of East Shewa Zone, Ethiopia," *Geology, Ecology, and Landscapes*, Taylor & Francis, vol. 6, no. 3, pp. 159–173, 2022. https://doi.org/10.1080/24749508.2020.1809059.

[12] M. A. Günen, "Determination of the suitable sites for constructing solar photovoltaic (PV) power plants in Kayseri, Turkey using GIS-based ranking and AHP methods," *Environmental Science and Pollution Research*, Springer, vol. 28, no. 40, pp. 57232–57247, 2021. https://doi.org/10.1007/s11356-021-14622-x.

[13] B. A. Ajanaku, M. P. Strager, and A. R. Collins, "GIS-based multi-criteria decision analysis of utility-scale wind farm site suitability in West Virginia," *GeoJournal*, Springer, vol. 87, no. 5, pp. 3735–3757, 2022. https://doi.org/10.1007/s10708-021-10453-y.

[14] Wang, Z., & Guo, J. "Adaptive Convolutional Residual Network for Dual-Task Forecasting in Energy Market Planning,"*Informatica*,vol. 49,no.24,pp. 39–54,2025.https://doi.org/10.31449/inf.v49i24.8032

[15] H. A. Effat and A. M. El-Zeiny, "Geospatial modeling for selection of optimum sites for hybrid solar-wind energy in Assiut Governorate, Egypt," *The Egyptian Journal of Remote Sensing and Space Science*, Elsevier, vol. 25, no. 2, pp. 627–637, 2022. https://doi.org/10.1016/j.ejrs.2022.03.005.

[16] M. S. Genç, F. Karipoğlu, K. Koca, and Ş. T. Azgın, "Suitable site selection for offshore wind farms in Turkey's seas: GIS-MCDM based approach," *Earth Sci Inform*, Springer, vol. 14, no. 3, pp. 1213–1225, 2021. https://doi.org/10.1007/s12145-021-00632-3.

[17] S. Zhao, Z. Xu, Z. Zhu, X. Liang, Z. Zhang, and R. Jiang, "Short and Long-Term Renewable Electricity Demand Forecasting Based on CNN-Bi-GRU Model," *ICCK Transactions on Emerging Topics in Artificial Intelligence*, ICJK, vol. 2, no. 1, pp. 1–15, 2025. https://doi.org/10.62762/TETAI.2024.532253.

[18] M. A. Hassaan, A. Hassan, and H. Al-Dashti, "GIS-based suitability analysis for siting solar power plants in Kuwait," *The Egyptian Journal of Remote Sensing and Space Science*, Elsevier, vol. 24, no. 3, pp. 453–461, 2021. https://doi.org/10.1016/j.ejrs.2020.11.004.

[19] M. Kacare, I. Pakere, A. Grāvelsiņš, and D. Blumberga, "Spatial analysis of renewable energy sources," *Rigas Tehniskas Universitates Zinatniskie Raksti*, Sciendo, vol. 25, no. 1, pp. 865–878, 2021. https://doi.org/10.2478/rtuect-2021-0065.

[20] S. Rekik and S. El Alimi, "A spatial perspective on renewable energy optimization: case study of southern Tunisia using GIS and multicriteria decision making," *Energy Exploration & Exploitation*, Sage Publications, vol. 42, no. 1, pp. 265–291, 2024. https://doi.org/10.1177/01445987231210962.

[21] X. Zhang, M. Xu, S. Wang, Y. Huang, and Z. Xie, "Mapping photovoltaic power plants in China using Landsat, random forest, and Google Earth Engine," *Earth Syst Sci Data*, vol. 14, no. 8, pp. 3743–3755, 2022. https://doi.org/10.5194/essd-14-3743-2022.

[22] B. Chauhan, R. Tabassum, S. Tomar, and A. Pal, "Analysis for the prediction of solar and wind generation in India using ARIMA, linear regression and random forest algorithms," *Wind Engineering*, Sage Publications, vol. 47, no. 2, pp. 251–265, 2023. https://doi.org/10.1177/0309524X221126742.

[23] D. Salman, C. Direkoglu, M. Kusaf, and M. Fahrioglu, “Hybrid deep learning models for time series forecasting of solar power,” *Neural Comput Appl*, Springer, vol. 36, no. 16, pp. 9095–9112, 2024. https://doi.org/10.1007/s00521-024-09558-5.

[24] T. Zheng, H. Li, H. He, Z. Lei, and S. Gao, “An Adaptive Strategy-incorporated Integer Genetic Algorithm for Wind Farm Layout Optimization,” *J Bionic Eng*, Springer, vol. 21, no. 3, pp. 1522–1540, 2024. https://doi.org/10.1007/s42235-024-00498-3.

[25] Y. Li, J. Li, and Y. Wang, “Privacy-preserving spatiotemporal scenario generation of renewable energies: A federated deep generative learning approach,” *IEEE Trans Industr Inform*, IEEE, vol. 18, no. 4, pp. 2310–2320, 2021. https://doi.org/10.1109/TII.2021.3098259.

[26] Y. Wang, Y. Li, H. Xie, B. Wu, and Y. Yang, “Cluster division in wind farm through ensemble modelling,” *IET Renewable Power Generation*, Wiley Online Library, vol. 16, no. 7, pp. 1299–1315, 2022. https://doi.org/10.1049/rpg2.12276.

[27] T. Zuo, Y. Zhang, K. Meng, Z. Tong, Z. Y. Dong, and Y. Fu, “A two-layer hybrid optimization approach for large-scale offshore wind farm collector system planning,” *IEEE Trans Industr Inform*, IEEE, vol. 17, no. 11, pp. 7433–7444, 2021. https://doi.org/10.1109/TII.2021.3056428.

[28] H. Eroğlu, “Multi-criteria decision analysis for wind power plant location selection based on fuzzy AHP and geographic information systems,” *Environ Dev Sustain*, Springer, vol. 23, no. 12, pp. 18278–18310, 2021. https://doi.org/10.1007/s10668-021-01438-5.

[29] M. Deveci, D. Pamucar, U. Cali, E. Kantar, K. Kölle, and J. O. Tande, “Hybrid q-rung orthopair fuzzy sets based CoCoSo model for floating offshore wind farm site selection in Norway,” *CSEE Journal of Power and Energy Systems*, CSEE, vol. 8, no. 5, pp. 1261–1280, 2022. https://doi.org/10.17775/CSEEJPES.2021.07700.

[30] X. Fu, X. Wu, C. Zhang, S. Fan, and N. Liu, “Planning of distributed renewable energy systems under uncertainty based on statistical machine learning,” *Protection and Control of Modern Power Systems*, PSPC, vol. 7, no. 4, pp. 1–27, 2022. https://doi.org/10.1186/s41601-022-00262-x.

[31] E. Tinsley, J. S. P. Froidevaux, S. Zsebők, K. L. Szabadi, and G. Jones, “Renewable energies and biodiversity: Impact of ground-mounted solar photovoltaic sites on bat activity,” *Journal of Applied Ecology*, Wiley Online Library, vol. 60, no. 9, pp. 1752–1762, 2023. https://doi.org/10.1111/1365-2664.14474.

[32] Q. Wang, Y. Ge, and R. Li, “Does improving economic efficiency reduce ecological footprint? The role of financial development, renewable energy, and industrialization,” *Energy & Environment*, Sage Publications, vol. 36, no. 2, pp. 729–755, 2025. https://doi.org/10.1177/0958305X231183914.

[33] M. Sahoo and N. Sethi, “The intermittent effects of renewable energy on ecological footprint: evidence from developing countries,” *Environmental Science and Pollution Research*, Springer, vol. 28, no. 40, pp. 56401–56417, 2021. https://doi.org/10.1007/s11356-021-14600-3.

[34] Y. Song, D. Tang, J. Yu, Z. Yu, and X. Li, “Short-term forecasting based on graph convolution networks and multiresolution convolution neural networks for wind power,” *IEEE Trans Industr Inform*, IEEE, vol. 19, no. 2, pp. 1691–1702, 2022. https://doi.org/10.1109/TII.2022.3176821.